Micro-spectroscopy of Buried Short-Range Surface Plasmon Polaritons Supported by Thin Polycrystalline Gold Films

Malte Großmann[1] · Maximilian Black[1] · Joris Jaruschewski[1] · Alwin Klick[1] · Till Leißner[2] · Jacek Fiutowski[2] · Horst-Günter Rubahn[2] · Michael Bauer[1]

Abstract
The dispersive properties of short-range surface plasmon polaritons are investigated at the buried interfaces in vacuum/Au/fused silica and vacuum/Au/SiO$_2$/Si multilayer systems for different gold film thicknesses of up to 50 nm using two-photon photoemission electron microscopy. The experimental data agrees excellently with results of transfer matrix method simulations, emphasizing the sensitivity of the plasmonic wave vector to the thickness of the gold film and an ultrathin native substrate oxide layer. The results furthermore illustrate the exceptional qualification of low-energy electron photoemission techniques in studying electronic excitations at buried interfaces.

Keywords Plasmonics · Surface plasmon polaritons · SPP · Short range plasmons · Buried interface

Surface plasmon polaritons (SPPs) are collective excitations of quasi-free electrons near a metal–dielectric interface coupled to an electromagnetic wave in the dielectric. They are strongly confined to their host interface but can freely propagate along it. Among their properties, they have one of particular importance: their wave vector for propagation along the interface is larger than the wave vector of light at the same frequency. Since the wave vector is inversely related to how narrowly a wave can be focused, this property allows for SPPs to be focused into smaller spaces than light. SPPs are therefore capable of bypassing the diffraction limit of light [1, 2]. In recent years, a number of studies were carried out exploiting this ability of SPPs to be confined into nanospaces for numerous applications, such as wavelength add-drop multiplexers [3], ring resonators and Bragg reflectors [4], bends and couplers [5, 6], and mechanically flexible nanophotonic waveguides [7]. On top of the all-optical methods used specifically to analyze performance of the devices in the previous works, such diverse methods as photon-induced near-field electron microscopy [8],

leakage radiation microscopy [9], scanning near-field optical microscopy [10], and photoemission electron microscopy (PEEM) [11–14] enabled the investigation of fundamental aspects of SPP propagation on the relevant length scales. While the previous discussion exclusively dealt with SPPs at metal-dielectric interfaces and in metal-dielectric structures, recent developments have expanded the scope of plasmonics to more exotic two-dimensional materials such as graphene [15–17] and black phosphorus [18]. The works showcase potential applications, namely highly tunable field-effect transistors [15] and metamaterials based on split-ring resonators [17], in the few THz regime, a frequency range known as the "THz gap" above the operation speed of electronics but below the speed of photonics.

A common sample design used for the study of SPPs consists of a metal film that is carried on a dielectric substrate. For simplicity's sake, we will limit the discussion to such cases where the metal surface is in contact with vacuum, leading to a sample system consisting of two interfaces: one between vacuum and metal and one between metal and substrate. Most commonly, the vacuum-metal interface and the SPP it can host are the focus of investigation. However, in general, it is also possible to excite SPPs at the buried metal-substrate interface. A typical sample for plasmonic studies therefore can house not only one but two SPP modes simultaneously. If the metal film becomes sufficiently thin, these modes influence the properties of each other. In such cases,

✉ Malte Großmann
grossmann@physik.uni-kiel.de

1 Institute of Experimental and Applied Physics, University of Kiel, Leibnizstr. 19, D-24118 Kiel, Germany

2 Mads Clausen Institute, NanoSYD, University of Southern Denmark, Alsion 2, DK-6400 Sønderborg, Denmark

they are referred to as long-range SPP (LR-SPP) and short-range SPP (SR-SPP), owing mostly to the difference in their attenuation that affords the LR-SPP a higher propagation distance along its interface. Except in the case of a symmetric dielectric environment, which results in the full hybridization of LR- and SR-SPP [19], the LR-SPP is localized at the metal-vacuum interface while the SR-SPP is localized at the buried metal-substrate interface. Due to this fact and their higher attenuation, SR-SPPs are typically more difficult to detect and there exist only few studies detecting both LR- and SR-SPP modes simultaneously [19–22]. Both types of SPP hold properties that are of interest for potential applications. On one hand, the LR-SPP innately has a higher propagation length than its SR-SPP counterpart. A number of theoretical and experimental studies concentrating on tailoring the LR-SPP to push this propagation length to the extreme can be found in [23–26]. On the other hand, if an appropriate substrate is used, the SR-SPP possesses a significantly higher wave vector than the LR-SPP and can therefore be confined into smaller spaces than the LR-SPP, bypassing the diffraction limit of light by an even higher margin. This property has for instance been used to fabricate highly integrated sensors [27, 28]. However, direct microscopic imaging of SR-SPP on metal films has become possible only recently: in a two-photon PEEM (2P-PEEM) experiment, providing a lateral resolution in the 10-nm range, Frank et al. experimentally demonstrated an SR-SPP sensitivity and confirmed the SR-SPP focusing capability associated with a high wave vector [20]. In their study, the authors used samples made of monocrystalline 20-nm-thick Au flakes on top of Si substrates with a 2.5-nm-thick native layer of SiO_2.

In this micro-spectroscopy study, we exploit the high sensitivity of 2P-PEEM to the plasmonic electric fields at and near the metal surface in combination with the high mean free path of low energy electrons to systematically investigate SR-SPP dispersion relations as a function of gold film thickness and for different substrates. Notably, even for polycrystalline gold and a film thickness of up to 50 nm, a high signal amplitude of the SR-SPP is observed. This becomes possible in part due to the usage of a novel rear-illumination operation mode of the used PEEM system [21]. An interpretation of the SR-SPP data is achieved through comparison with numerical simulations proving the high sensitivity of the SR-SPP wave vector to subtle changes in the dielectric environment.

Experimental Setup and Simulations

The micro-spectroscopy experiments were conducted using a photoemission electron microscope (IS PEEM, Focus GmbH) [29] mounted in an ultrahigh vacuum (UHV) μ-metal chamber and providing a lateral resolution of 40 nm. Two

different experimental schemes were used: in the first experimental scheme, the sample was excited under a fixed angle of incidence of 0° toward the sample surface normal by transform-limited laser pulses (< 100-fs pulse width) from a Ti:Sapphire oscillator which is operated at a repetition rate of 80 MHz (Tsunami, Spectra Physics) (see Fig. 1a). Excitation is carried out by illumination from the rear side through the transparent sample substrate utilizing a special focusing setup [21]. In this case, the sample (sample 1) is a 50-nm-thick gold film fabricated by magnetron sputtering on top of a 1-mm-thick fused silica (SiO_2) wafer. The sputtering process exhibits no constraints on crystal growth, leading to the formation of a polycrystalline film with arbitrary grain orientation. Due to an excellent agreement of our current and past experimental findings (e.g., [30]) if permittivity data for evaporated gold from [31] is used, we expect a morphology similar to the one discussed by Olmon and coworkers in that publication. In the second experimental scheme, the sample was excited from the front side under a fixed angle of incidence of 65° toward the sample surface normal by
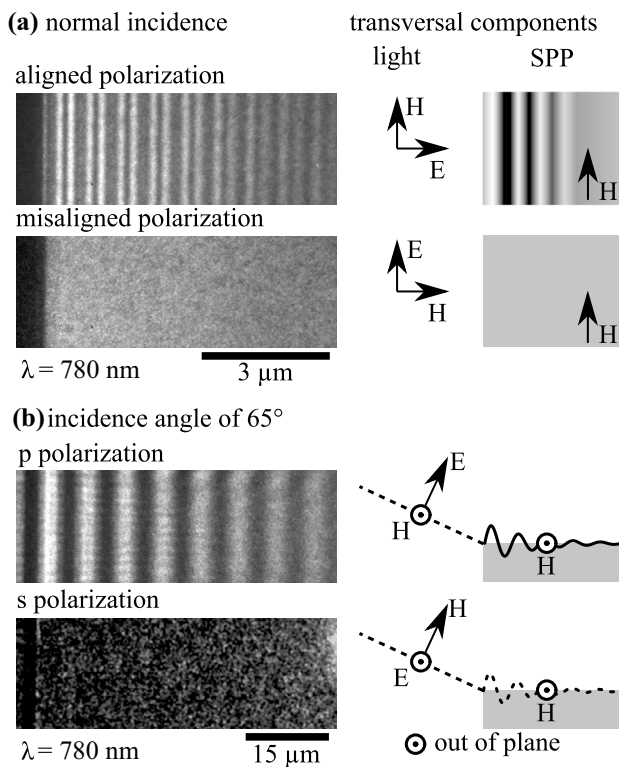
(a) *sample 1*

(b) *sample 2 and 3*
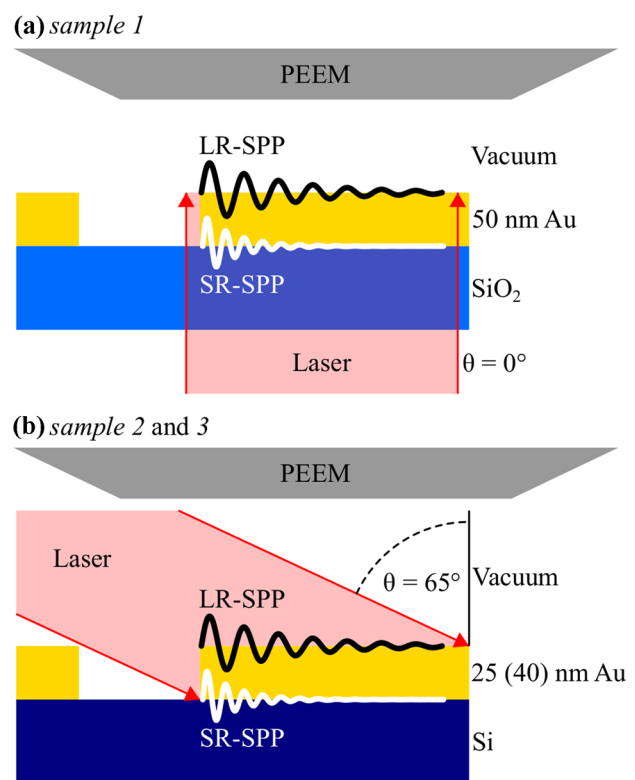
Fig. 1 Scheme of illumination and detection geometry. (**a**) Sample 1 illuminated by the laser under normal incidence from the sample rear side. Relevant sample parameters are indicated. (**b**) Sample 2 (sample 3) illuminated by the laser under oblique incidence from the sample front side. Relevant sample parameters are indicated. In both images, the gaps in the gold films indicate the 4-μm-wide slits fabricated through FIB and providing coupling edges for SPP excitation using NIR laser pulses

the same transform-limited laser pulses (see Fig. 1b). In this case, the samples are a 25 nm (sample 2) and a 40 nm (sample 3) thick polycrystalline gold film fabricated as before on top of a 0.5-mm-thick silicon wafer. The surface of the silicon wafer is covered by a native oxide layer of a few nm thickness. As will be discussed below, an accurate determination of the layer thickness becomes possible from the analysis of the experimental data from samples 2 and 3. In both cases, the transversal magnetic (TM) component of the incident transversal electromagnetic (TEM) light wave has to be aligned with the transversal magnetic field of the purely TM SPP wave in order to achieve an excitation of the SPP. For normal incidence, both transversal components of the TEM light wave are in the sample surface. In this case, the magnetic field has to be aligned perpendicular to the propagation direction of the SPP wave (see Fig. 2a). For an angle of incidence of 65°, we differentiate between two polarization cases: one where the transversal electric component of the incident TEM light wave is parallel to the plane given by the propagation direction of light and the surface normal (p polarization) and one where it is perpendicular to this plane

Fig. 2 Scheme of polarization matching necessary for the excitation of plasmons. (**a**) Polarization scheme used in normal incidence (sample 1). (**b**) Polarization scheme used for incidence with an angle of 65° (samples 2 and 3). On the right-hand side, the vectors (E for electric field and H for magnetic field) for the transversal components of incident light and SPP are given. The PEEM images on the left-hand side were taken on sample 1

(s polarization). The magnetic component of the TEM light wave is only aligned to the TM SPP wave if we have p polarization (see Fig. 2b). In the experiments, the near-infrared (NIR) central laser wavelength was continuously tunable between 710 and 890 nm ($h\nu$ = 1.4–1.7 eV) and it was measured using a calibrated fiber optic spectrometer (USB4000, Ocean Optics) in front of the UHV chamber entrance window. Prior to the photoemission measurements, the samples were covered with a small amount of cesium (coverage << 1 monolayer) by in situ treatment using a well-degassed getter source (Cs dispenser, SAES Getters). This treatment is required to lower the work function in order to facilitate a two-photon photoemission (2PPE) process with the near-infrared laser pulses. SPP propagation (real and imaginary part of the SPP wave vector) is not affected in the applied coverage regime within the resolution of our experiment [30]. PEEM image analysis was done using the software Fiji [32]. The software used to control the CCD camera of the experimental setup is μManager [33]. Reference sample images were taken in conventional threshold PEEM (T-PEEM) and helium ion microscopy (HIM). For T-PEEM, the excitation source was a Hg discharge lamp ($h\nu$ = 4.9 eV). HIM was carried out by an Orion NanoFab helium ion microscope (Carl Zeiss) at 25-keV beam energy, with a probe current ranging from 0.5 to 1.1 pA. In order to preserve the sample surface information, no conductive coatings were applied to the samples prior to imaging [34]. The same instrument operated at a beam energy of 30 kV and a beam current of approximately 70 pA was used to fabricate 4 μm wide slits via gallium-focused ion beam lithography (FIB) providing defined edges for excitation of LR- and SR-SPP [35]. These slits are indicated as gaps in the gold coating in the schemes presented in Fig. 1. Additionally, periodic structures consisting of an array of 2 μm wide slits with 3-μm separation were milled into the gold film for length calibration.

Simulations of LR- and SR-SPP dispersion relations in the different sample systems were carried out using a transfer matrix method. This method allows for the calculation of a matrix relating the incoming and outgoing electromagnetic waves—so incident, reflected and transmitted waves—in the semi-infinite media above and below a stack of an arbitrary number of finite-thickness layers to one another. From this matrix, one can obtain the Fresnel coefficient of reflection for the entire stack. Surface modes, such as the SPP, cause anomalies in the value of this coefficient, leading to zeros or poles [36]. In our approach, we calculate the reflection coefficient for a wide range of input wave vectors and determine the wave vectors corresponding to a surface mode by finding local extrema in the calculated values of the coefficient. These extrema are caused by the anomalies. This approach allows the determination of the sought wave vectors on a current generation office computer with computation times of a few hours. Before we discuss detailed parameters used
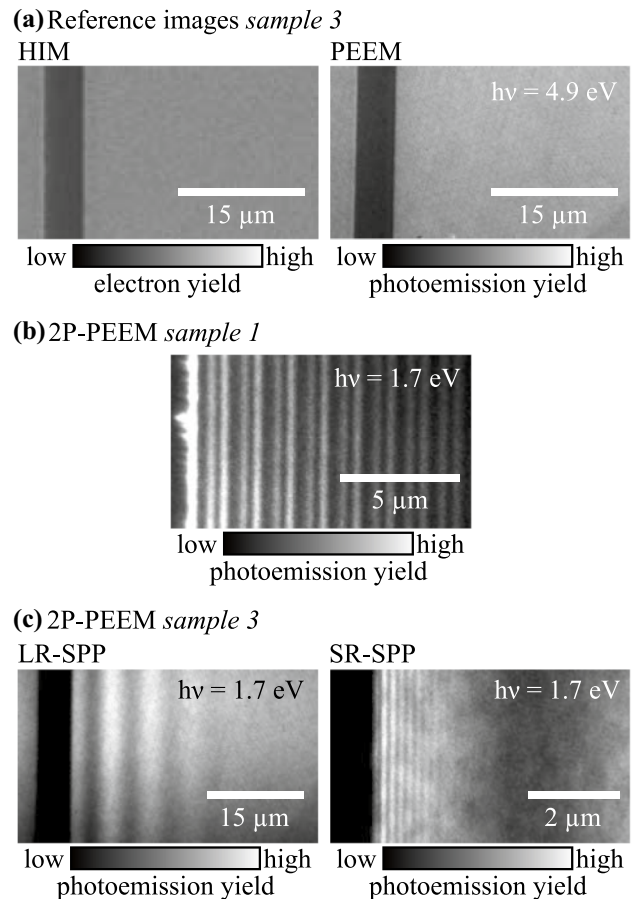
in our simulations, we would like to point out that we expect to find at least two modes for each interface in a dielectric-metal-dielectric structure: one corresponds to a mode that is able to radiate light on the far side of the inner metal layer while the other is evanescent in all media. Both modes are evanescent in the dielectric medium directly adjacent to the given interface. For more details on this subject and the physical interpretation of these modes, please refer to [37, 38]. Additionally, detailed descriptions of the calculation of transfer matrices and how to use them to find electromagnetic modes can be found in [38, 39]. In the following, we will give the parameters used in our simulations: the frequency resolution used in all cases was 0.05 fs^{-1}. In the simulations for sample 1, we used permittivity data from Ref. [31] for Au (evaporated gold, EV) and data from Ref. [40] for fused silica. The used wave vector resolution was 0.001 μm^{-1}. In the simulations for samples 2 and 3, we again used data from Ref. [31] for Au (EV) and data from Ref. [41] for Si. To account for the permittivity of the thin native oxide layer, we used permittivity data for SiO_2 from [42]. Note, however, that this has to be considered as an approximation as the chemical composition of a native oxide is in general complex [43–46]. Reference [47] lists 4 nm as the upper bound of the native oxide layer thickness of silicon, while Ref. [45] indicates a thickness of 1.2 nm after exposure to ambient conditions for approximately 100 min, a time far exceeded for the wafers used in the present experiment. Within this range, the thickness of the native oxide layer was set as a free parameter in the simulations to finally achieve agreement with the experimental data. In the simulations for samples 2 and 3, two different ranges were used for the LR-SPP and SR-SPP simulations in order to achieve a higher wave vector resolution. Here, the wave vector resolution for the LR-SPP was 0.0015 μm^{-1} and the resolution for the SR-SPP was 0.01 μm^{-1}.

Results and Discussion

Figure 3a shows HIM and T-PEEM images of sample 3 near the SPP coupling edge. A clear contrast between a dark and a light area is visible on the left side of the picture. The dark area marks the exposed substrate, where the gold coating (bright area) has been milled away by FIB. Figure 3b and c show 2P-PEEM images of sample 1 and sample 3, respectively, recorded upon excitation with 730-nm laser pulses. In Fig. 3b, SPP excitation is achieved with the laser pulses incident parallel to the surface normal from the sample rear side. In Fig. 3c, the laser pulses hit the front side of the sample from the left under an incidence angle of 65° to the surface normal. In both cases, we observe periodic signal patterns starting at the SPP coupling edge. These patterns originate from the superposition of the illuminating laser field and the SPP polarization

(a) Reference images *sample 3*

HIM   PEEM

low   high   low   high
electron yield   photoemission yield

(b) 2P-PEEM *sample 1*

hν = 1.7 eV

low   high
photoemission yield

(c) 2P-PEEM *sample 3*

LR-SPP   SR-SPP

hν = 1.7 eV   hν = 1.7 eV

low   high   low   high
photoemission yield   photoemission yield

Fig. 3 Microscopy images of the investigated samples. (**a**) Reference HIM and T-PEEM images of sample 3 showing the FIB-created slit providing defined edges for SPP excitation with the laser. (**b**) 2P-PEEM image showcasing the superposition pattern of LR-SPP and SR-SPP observed on sample 1. (**c**) 2P-PEEM images showcasing the LR-SPP signature (left) and SR-SPP signature (right) observed on sample 3. The images shown in (**b**) and (**c**) were recorded with a laser wavelength of 730 nm

field [11, 30]. Their periodicities arise from the wave vector mismatch $\Delta k = k_{SPP} - k_{exc}$ between laser and SPP with k_{exc} being the surface projected wave vector of the excitation laser and k_{SPP} being the real part of the wave vector of the SPP. Note that in the normal incidence excitation geometry, the surface projection of the laser wave vector vanishes, yielding the special case $k_{exc} = 0$ and $\Delta k = k_{SPP}$. The quantitative analysis of the patterns as a function of excitation wavelength allows determining the SPP dispersion relation, $\omega(k_{SPP})$. It is worth noting that because the observed periodicities arise due to Δk, the SPP wave vector in the oblique incidence excitation geometry leads to an intensity peak at Δk rather than at k_{SPP} upon Fourier transform of the measurement signal. Therefore, in the case of sample 2 and sample 3, we do not plot the spectra against the wave vector k obtained naturally from a Fourier transform. Rather, we plot the spectra against $(k + k_{exc})$. Due
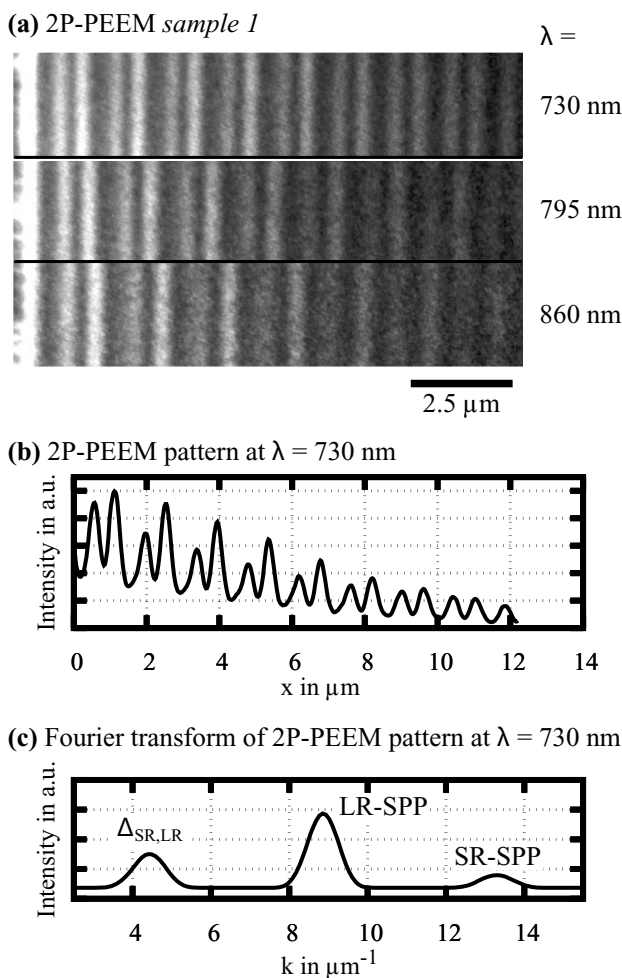
to this, the SPP signal leads to a peak at k_{SPP}, resulting in a more intuitive picture.

Figure 4a compares periodic signal patterns emerging from the SPP coupling edge for three different excitation wavelengths. We observe a clear change of the pattern periodicities, indicative for the dispersive character of the excited SPPs. Notably, the signal modulation of the pattern shows some complexity as is readily apparent in the 2PPE intensity profile in Fig. 4b, which has been obtained by integration of the top pattern shown in Fig. 4a along the vertical direction. We assign the appearance of this unconventional signal modulation to multiple wave vector mismatch components Δk superimposing on one another within the pattern. This is confirmed by a Fourier transform of the pattern (see Fig. 4c) that reveals three distinct wave vector components being involved in the

(a) 2P-PEEM *sample 1*

λ =

730 nm

795 nm

860 nm

2.5 µm

(b) 2P-PEEM pattern at λ = 730 nm

(c) Fourier transform of 2P-PEEM pattern at λ = 730 nm

Fig. 4 Detection and analysis of LR- and SR-SPP signals for sample 1. (**a**) 2P-PEEM data near the SPP coupling edge recorded at three different excitation wavelengths highlighting the dispersive nature of the SPP modes. (**b**) 2PPE intensity profile as a function of distance x from the coupling edge at λ = 730 nm extracted from the 2P-PEEM pattern shown in (**a**). (**c**) Fourier transform of the 2PPE intensity pattern shown in (**b**)

formation of the pattern. The comparison with our simulations and results from previous experiments [20, 30] implies that the signal peak at $k_{SPP} \approx 8.9$ µm^{-1} is due to the LR-SPP excited at the Au/vacuum-interface and that the peak at $k_{SPP} \approx 13.3$ µm^{-1} is due to the SR-SPP excited at the Au/SiO$_2$-interface. The distinct signal of the SR-SPP in the spectra which amounts to almost 30% of the LR-SPP amplitude highlights the high sensitivity of the experiment even to excitations that are localized at an interface buried below a 50-nm-thick polycrystalline gold film. The detection of such a strong signal is potentially assisted by the rear side illumination geometry used in this experiment [21]: the laser pulses incident from the sample rear side hit the buried interface before they are transmitted through and partly absorbed by the gold film. This implies a stronger and preferential excitation of the SR-SPP over the LR-SPP at least partly compensating for a reduced photoemission signal due to the finite mean free path of photoexcited electrons in the gold film [48]. We finally want to comment on the third peak in the Fourier spectrum, $\Delta_{SR,LR}$, which appears at $k \approx 4.4$ µm^{-1}. The value exactly matches the difference of the SR-SPP and LR-SPP wave vector peaks. We assume that this difference signal either originates from the non-linearity of the 2PPE detection process or alternatively from a residual coupling of LR- and SR-SPP [39].

Figure 5a shows a waterfall plot of Fourier spectra obtained from 2PPE intensity profiles recorded at different excitation wavelengths. We extract the dispersion relations for the LR-SPP and the SR-SPP from this data by determining the values of k_{SPP} from a Gaussian fit to the LR-SPP and SR-SPP signal peak for each spectrum. The dispersion relations obtained from the analysis of 2P-PEEM data from two identical samples (sample 1A and sample 1B) are shown in Fig. 5b in comparison to the results of our simulations (dashed lines). The very good agreement between measurement and simulations confirms the assignment of the two peaks to LR-SPP and SR-SPP and once again highlights the exceptional signal quality at which the buried SPP mode can be investigated with the used detection geometry.

In the following, we will present the 2P-PEEM data of sample 2 and sample 3. The results of our simulations for these sample geometries imply a substantially larger difference in the wave vectors between LR-SPP and SR-SPP than for sample 1. Correspondingly, also the 2P-PEEM signal periodicity determined by the wave vector mismatch Δk will differ considerably. In the experiment, LR-SPP and SR-SPP can therefore only be probed separately using different magnification settings of the PEEM instrument. Figure 6a shows 2P-PEEM data of sample 3 taken at three different wavelengths and for two different magnification settings of the PEEM optics, matching the pattern periodicity of the LR-SPP (left) and the SR-SPP (right). 2PPE intensity profiles of the 720 nm data (Fig. 6b) confirm that each dataset is governed by a single periodicity that we associate with the excitation of

(a)

(b)

| *sample 1A* ☐ | *sample 1B* ◇ | Simulation - - - |
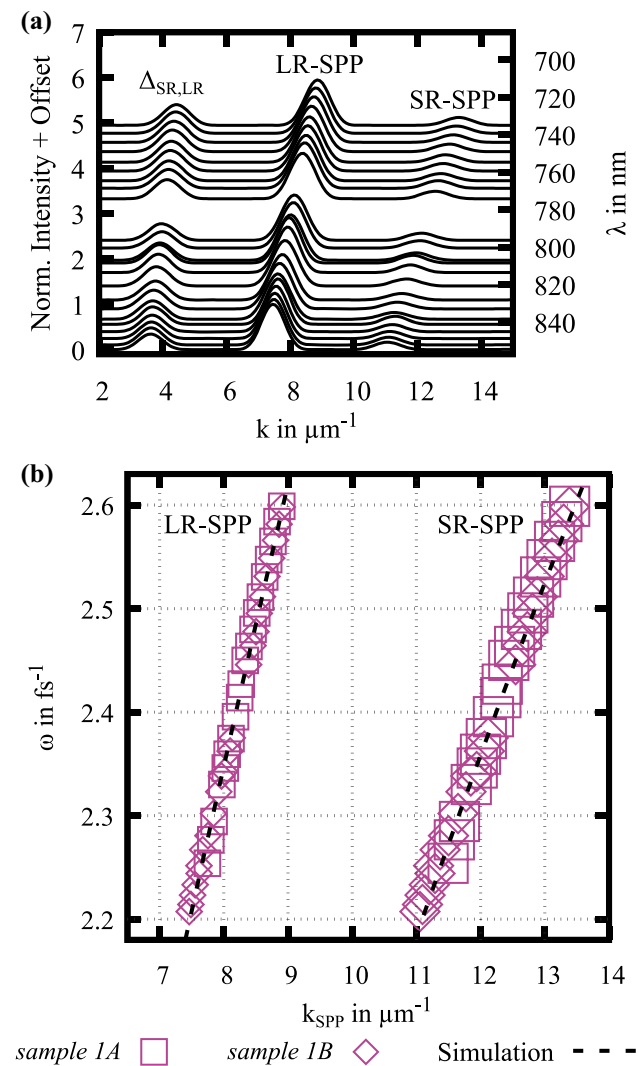
Fig. 5 LR-SPP and SR-SPP dispersion relations of sample 1. (**a**) Waterfall plot of Fourier spectra of 2PPE intensity profiles recorded upon excitation with different laser wavelength. The three peaks in each spectrum represent from left to right the difference signal from LR-SPP and SR-SPP ($\Delta_{SR,LR}$), the signal from the LR-SPP mode, and the signal from the SR-SPP mode. The baseline of each spectrum is aligned by excitation wavelength on the right-hand axis. (**b**) LR-SPP and SR-SPP dispersion relations obtained from measurements of two samples (sample 1A and sample 1B) in comparison with results of transfer matrix simulations (dashed lines). The systematic error of the length calibration as well as the statistical uncertainty of the Gaussian fit to the spectra is within the marker size

LR-SPP and SR-SPP, respectively. Notably, it is also possible to detect the buried interface plasmon in this experimental geometry. Note, however, that even though the thickness of the gold films is reduced in comparison to sample 1, the relative signal amplitude from the SR-SPP is now much smaller at least for the 40-nm-thick film, amounting to only 10% of the signal amplitude from the LR-SPP. This highlights the impact of the rear side illumination. For the 25-nm-thick

(a) 2P-PEEM *sample 3*

(b) 2P-PEEM patterns of *sample 3* at λ = 720 nm
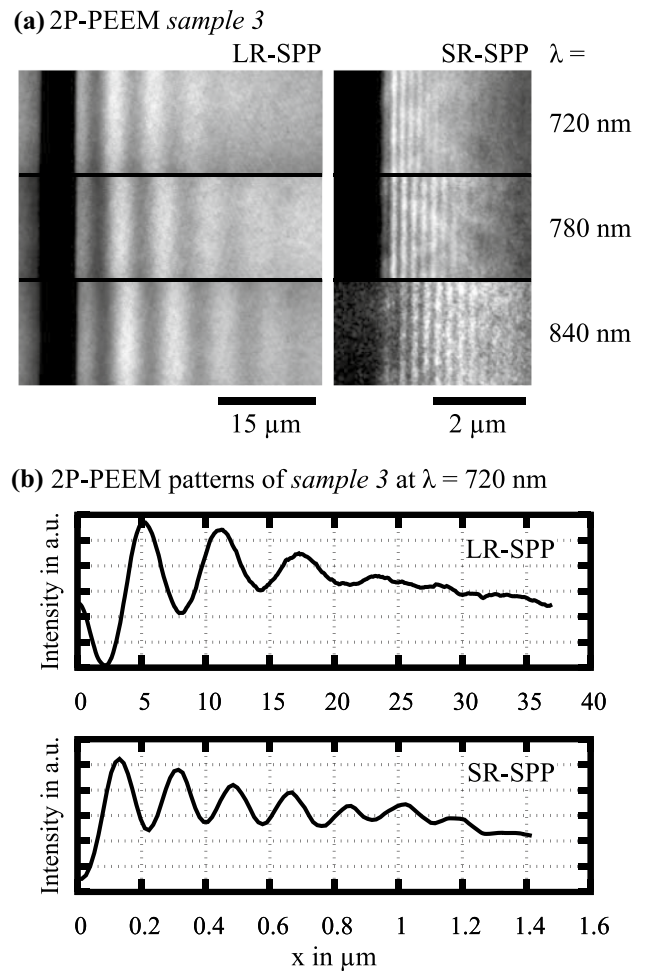
Fig. 6 Detection and analysis of LR- and SR-SPP signals for sample 3. (**a**) LR-SPP signal patterns (left) and SR-SPP signal patterns (right) at three different excitation wavelengths highlighting the dispersive nature of the SPP modes. (**b**) 2PPE intensity patterns for LR- and SR-SPP at λ = 720 nm extracted from the top pictures shown in (**a**)
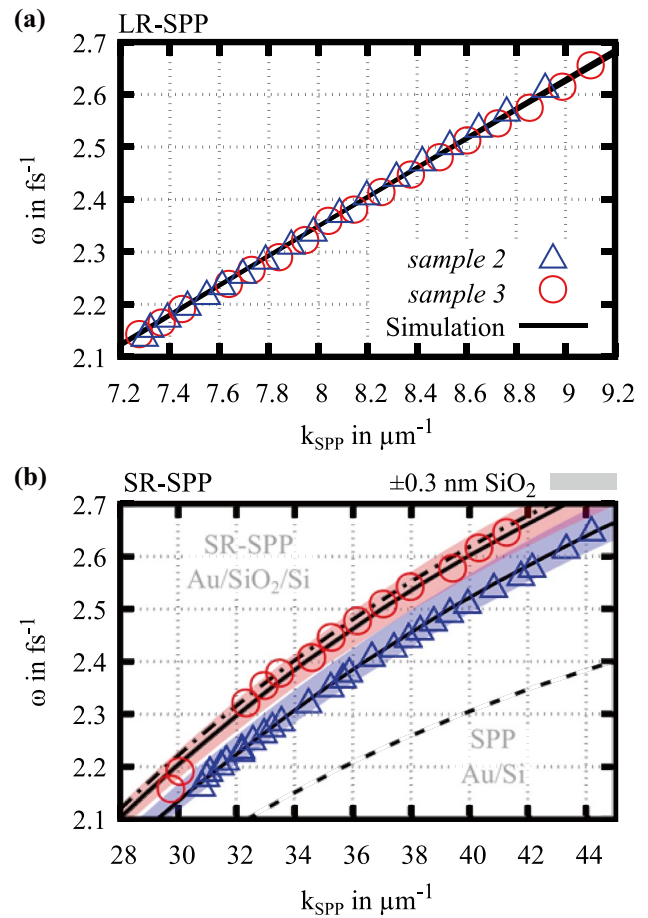
coating, the exponential dependence of the evanescent fields on thickness takes over, resulting in an SR-SPP amplitude that is roughly 50% of the LR-SPP.

Fourier spectra of 2PPE intensity profiles of sample 2 and sample 3 for different excitation wavelengths and covering the relevant wave vector range of LR-SPP (left) and SR-SPP (right) are plotted in Fig. 7a and b. As for sample 1, the dispersion relations are determined from Gaussian fits to the spectra. Figure 8 compares the results for sample 2 and sample 3 with the dispersion relations for the LR-SPP shown in Fig. 8a and for the SR-SPP shown in Fig. 8b. Additionally, the data are overlaid with the results of our simulations (solid lines). For the simulations, we adjusted the thickness of the native oxide layer for best agreement with the experimental data, yielding a thickness of 2 ± 0.3 nm. Clear differences in the dispersion relations as a function of film thickness are observed for the SR-SPP, whereas within
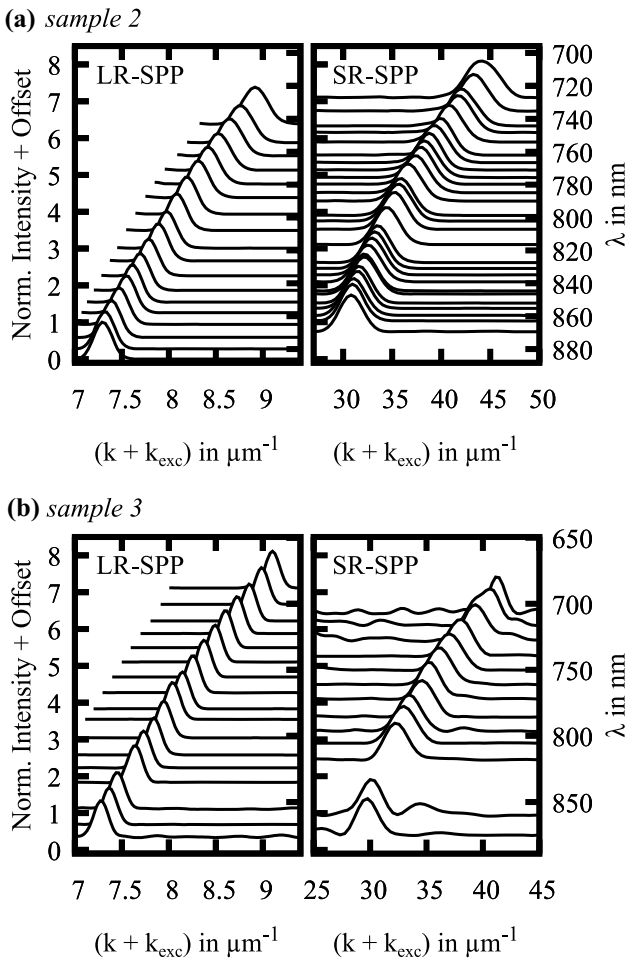
Fig. 7 Compilation of Fourier transformed data of sample 2 and sample 3. (**a**) Waterfall plot of Fourier spectra of the LR-SPP 2PPE intensity pattern (left) and of the SR-SPP 2PPE intensity pattern (right) of sample 2. (**b**) Waterfall plot of Fourier spectra of the LR-SPP 2PPE intensity pattern (left) and of the SR-SPP 2PPE intensity pattern (right) of sample 3. The baseline of each spectrum is aligned by excitation wavelength on the right-hand axis

Fig. 8 Comparison of LR-SPP and SR-SPP dispersion relations of sample 2 and sample 3. (**a**) Experimental dispersion relation for LR-SPP on the 25 nm gold coating (sample 2, blue triangles) and on the 40 nm gold coating (sample 3, red circles). Simulated dispersion relations for both gold film thicknesses are included (solid lines). There is no difference between the simulated dispersion relations on a scale that is significant for the experiment. (**b**) Experimental dispersion relations for the SR-SPP on the 25 nm gold coating (sample 2, blue triangles) and on the 40 nm gold coating (sample 3, red circles). Simulated dispersion relations for both gold film thicknesses are included (dashed lines) surrounded by shaded areas (blue for sample 2 and red for sample 3) marking the simulated effect of a ± 0.3 nm native oxide layer thickness variation. For comparison, the simulated SPP dispersion relations in an $Au/SiO_2/Si$-system (black dash-dotted line) and at an isolated Au/Si-interface (black dashed line) are added. In both graphs, the statistical uncertainty obtained from the fit algorithm is smaller than the marker size

the experimental resolution the dispersion of the LR-SPP seems to be not affected by the gold film thickness at all. This striking difference between LR-SPP and SR-SPP is a direct consequence of the asymmetry in the dielectric environment formed by superstrate (vacuum, $\varepsilon = 1$) and substrate (SiO_2/Si, $\varepsilon > 1$): at any interface the SPP electric field components must fulfill continuity conditions. For a purely single interface system, this condition can be fulfilled by an SPP propagating along the interface and exponentially decaying perpendicular to the interface into both adjacent mediums. This field configuration is schematically illustrated in Fig. 9a. For a three-layer system and a sufficiently small metal film thickness, the field configuration of the SPP must change to comply with the continuity conditions now to be fulfilled at both interfaces. For the LR-SPP, which is localized at the vacuum-metal interface, the field decaying

into the metal eventually encounters the dielectric substrate. Since the permittivity of the substrate is higher than that of vacuum, the field is no longer evanescent and can instead be radiated into the substrate as light. This phenomenon is known as "leakage radiation" [49]. The light-like nature of the fields in the substrate introduces an additional degree of freedom: the emission angle γ. The resulting field configuration is schematically depicted in Fig. 9b. The emission angle trivializes fulfilling the continuity conditions at the

(a) Single interface
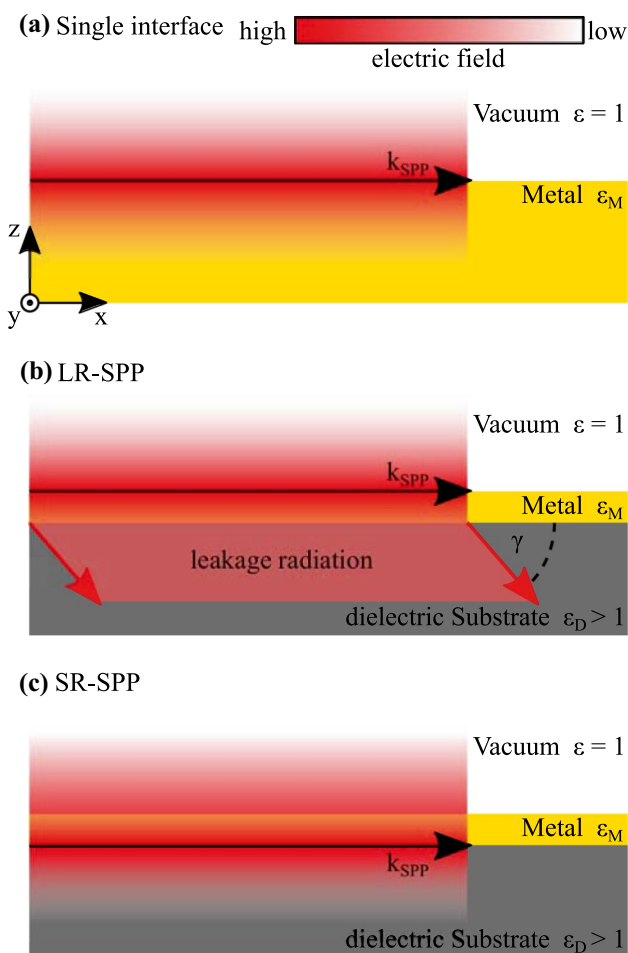
(b) LR-SPP

(c) SR-SPP

Fig. 9 Schematic illustration of the electric fields of an SPP at a single interface (**a**), an LR-SPP (**b**), and an SR-SPP (**c**). The coordinate system in the lower left of (**a**) and the electric field scale bar in the top right of (**a**) are valid for all three graphs

metal-substrate interface. Therefore, the LR-SPP properties are mostly defined by the conditions at the vacuum-metal interface and do not strongly depend on the metal film thickness. For the SR-SPP, however, the field decaying into the metal eventually encounters vacuum due to its localization at the metal-substrate interface. Here, leakage radiation cannot occur due to the permittivity of vacuum being lower than that of the substrate. The field is evanescent in all media and no additional degree of freedom can soften the boundary conditions. This field configuration is depicted in Fig. 9c. The SR-SPP must accommodate both sets of continuity conditions. The critical parameter is the remaining field strength at the gold-vacuum interface, which depends exponentially on the gold film thickness. This explains the strong thickness dependence of the SR-SPP dispersion.

For comparison, we added in Fig. 8b the simulated dispersion relation of an SPP in an Au/Si-system with a 2-nm-thick native SiO_2 layer at the interface (black dash-dotted line). This line marks the decoupled case where an infinite metal

thickness fully separates the SPP modes. From this comparison, it becomes apparent that in the present system, the SR-SPP already behaves almost like a decoupled SPP when separated from the vacuum-metal interface by a 40-nm-thick Au film.

As a final remark, we would like to emphasize the strong effect of the ultrathin native oxide layer of sample 2 and sample 3 onto the SR-SPP dispersion relation and conversely the sensitivity of the SR-SPP to the immediate vicinity of the buried interface. Figure 8b includes shaded areas near the simulation results (blue for sample 2 and red for sample 3) that indicate the change of the simulated dispersion upon variation of the native oxide layer thickness by ± 0.3 nm. These areas fully encompass the experimental results, implying that from the experimental data, the native oxide layer thickness can be determined at the accuracy of state-of-the-art spectroscopic ellipsometry techniques [50]. However, such an accuracy can only be achieved for bare surfaces in the latter case. In Fig. 8b, we also added simulation results of the SPP dispersion relation for an isolated Au/Si interface (black dashed line). Without a native oxide layer, the SR-SPP of the Si/Au/vacuum systems should closely follow this dispersion. In comparison to the experimental data, we observe in the probed frequency range an increase of k_{SPP} of up to 50%. The effect of the SiO_2 can be further understood when comparing these results with the observations on sample 1. The SR-SPP on sample 1 is in principle the SR-SPP of a SiO_2/Au/vacuum system—with some deviation due to the differences in permittivity between fused silica and native SiO_2. Further increasing the SiO_2-layer thickness can therefore in the extreme reduce k_{SPP} to roughly a third of the values observed on sample 2 and sample 3.

Conclusions

We presented a systematic PEEM study of the SR-SPP dispersion relation at different buried gold-dielectric interfaces. We demonstrated the high sensitivity of PEEM to plasmonic modes not only at exposed interfaces but also at interfaces buried by polycrystalline gold films of thicknesses up to 50 nm. This is achieved in part through the usage of a rear side illumination setup [21]. We provided experimental data on how the SR-SPP dispersion is affected by the gold film thickness and the substrate properties, including very small thickness variations of ultrathin native oxide layers. We would like to emphasize particularly this last point, as the observed drastic impact of such an interlayer with a thickness of only 2 nm could lend itself to manipulate the dispersive properties of SR-SPP to suit ones needs. This potential fine tuning capability combined with a wave vector that is larger than that of the LR-SPP makes the SR-SPP a potential candidate

for advancements in applications where a large wave vector is highly critical to push the diffraction limit—and thus, imaging resolution—to its extreme, such as plasmon microscopy [51].

Data Availability The material and data that this work is based upon is available from the corresponding author upon reasonable request.

Compliance with Ethical Standards

Conflict of Interest The authors declare that they have no competing interests.

Consent to Participate Informed consent was obtained from all authors.

Consent to Publish The authors confirm that there is informed consent to the publication of the data contained in the article.

References

1. Barnes WL, Dereux A, Ebbesen TW (2003) Surface Plasmon Subwavelength Optics. Nature 424:824–830. https://doi.org/10.1038/nature01937
2. Gramotnev DK, Bozhevolnyi SI (2010) Plasmonics Beyond the Diffraction Limit. Nat Photonics 4:83–91. https://doi.org/10.1038/nphoton.2009.282
3. Biagi G, Fiutowski J, Radko IP et al (2015) Compact Wavelength Add–drop Multiplexers Using Bragg Gratings in Coupled Dielectric-loaded Plasmonic Waveguides. Opt Lett 40:2429. https://doi.org/10.1364/OL.40.002429
4. Krasavin AV, Zayats AV (2010) All-optical Active Components for Dielectric-loaded Plasmonic Waveguides. Opt Commun 283:1581–1584. https://doi.org/10.1016/j.optcom.2009.08.054
5. Charbonneau R, Lahoud N, Mattiussi G, Berini P (2005) Demonstration of Integrated Optics Elements Based on Long-ranging Surface Plasmon Polaritons. Opt Express 13:977–984. https://doi.org/10.1364/OPEX.13.000977
6. Steinberger B, Hohenau A, Ditlbacher H et al (2007) Dielectric Stripes on Gold as Surface Plasmon Waveguides: Bends and Directional Couplers. Appl Phys Lett 91:1–3. https://doi.org/10.1063/1.2772774
7. Vernoux C, Chen Y, Markey L et al (2018) Flexible Long-range Surface Plasmon Polariton Single-mode Waveguide for Optical Interconnects. Opt Mater Express 8:469. https://doi.org/10.1364/OME.8.000469
8. Lummen TTA, Lamb RJ, Berruto G et al (2016) Imaging and Controlling Plasmonic Interference Fields at Buried Interfaces. Nat Commun 7:1–9. https://doi.org/10.1038/ncomms13156
9. Birr T, Fischer T, Evlyukhin AB et al (2017) Phase-resolved Observation of the Gouy Phase Shift of Surface Plasmon Polaritons. ACS Photonics 4. https://doi.org/10.1021/acsphotonics.6b00999
10. Dvořák P, Neuman T, Břínek L et al (2013) Control and Near-field Detection of Surface Plasmon Interference Patterns. Nano Lett 13:2558–2563. https://doi.org/10.1021/nl400644r
11. Kubo A, Pontius N, Petek H (2007) Femtosecond Microscopy of Surface Plasmon Polariton Wave Packet Evolution at the Silver/Vacuum Interface. Nano Lett 7:470–475. https://doi.org/10.1021/nl0627846
12. Kahl P, Podbiel D, Schneider C et al (2018) Direct Observation of Surface Plasmon Polariton Propagation and Interference by Time-resolved Imaging in Normal-incidence Two Photon Photoemission Microscopy. Plasmonics 13:239–246. https://doi.org/10.1007/s11468-017-0504-6
13. Lemke C, Leißner T, Evlyukhin A et al (2014) The Interplay Between Localized and Propagating Plasmonic Excitations Tracked in Space and Time. Nano Lett 14:2431–2435. https://doi.org/10.1021/nl500106z
14. Podbiel D, Kahl P, Makris A et al (2017) Imaging the Nonlinear Plasmoemission Dynamics of Electrons from Strong Plasmonic Fields. Nano Lett 17:6569–6574. https://doi.org/10.1021/acs.nanolett.7b02235
15. Wang L, Chen X, Yu A et al (2014) Highly Sensitive and Wide-band Tunable Terahertz Response of Plasma Waves Based on Graphene Field Effect Transistors. Sci Rep 4:1–8. https://doi.org/10.1038/srep05470
16. Ni GX, Wang L, Goldflam MD et al (2016) Ultrafast Optical Switching of Infrared Plasmon Polaritons in High-mobility Graphene. Nat Photonics 10:244–247. https://doi.org/10.1038/nphoton.2016.45
17. Tang W, Wang L, Chen X et al (2016) Dynamic Metamaterial Based on the Graphene Split Ring High-Q Fano-resonnator for Sensing Applications. Nanoscale 8:15196–15204. https://doi.org/10.1039/c6nr02321e
18. Ni X, Wang L, Zhu J et al (2017) Surface Plasmons in a Nanostructured Black Phosphorus Flake. Opt Lett 42:2659. https://doi.org/10.1364/OL.42.002659
19. Pettit RB, Silcox J, Vincent R (1975) Measurement of Surface-plasmon Dispersion in Oxidized Aluminum Films. Phys Rev B 11:3116–3123. https://doi.org/10.1103/PhysRevB.11.3116
20. Frank B, Kahl P, Podbiel D et al (2017) Short-range Surface Plasmonics: Localized Electron Emission Dynamics from a 60-nm

Spot on an Atomically Flat Single-crystalline Gold Surface. Sci Adv 3:e1700721. https://doi.org/10.1126/sciadv.1700721

21. Klick A, Großmann M, Beewen M et al (2019) Femtosecond Time-resolved Photoemission Electron Microscopy Operated at Sample Illumination from the Rear Side. Rev Sci Instrum 90:053704. https://doi.org/10.1063/1.5088031

22. Li Y, Zhang H, Zhu N et al (2011) Short-range Surface Plasmon Propagation Supported by Stimulated Amplification using Electrical Injection. Opt Express 19:22107. https://doi.org/10.1364/OE.19.022107

23. Wendler L, Haupt R (1986) Long-range Surface Plasmon-polaritons in Asymmetric Layer Structures. J Appl Phys 59:3289–3291. https://doi.org/10.1063/1.336884

24. Jian-Jun C, Zhi L, Qi-Huang G (2009) Long-range Surface Plasmon Polaritons with Subwavelength Mode Expansion in an Asymmetrical System. Chinese Phys B 18:3535–3541. https://doi.org/10.1088/1674-1056/18/8/066

25. Dohi H, Kuwamura Y, Fukui M, Tada O (1984) Long-range Surface Plasmon Polaritons in Metal Films Bounded by Similar-refractive-index Materials. J Phys Soc Japan 53:2828–2832. https://doi.org/10.1143/JPSJ.53.2828

26. Konopsky VN, Alieva EV (2006) Long-range Propagation of Plasmon Polaritons in a Thin Metal Film on a One-dimensional Photonic Crystal Surface. Phys Rev Lett 97:1–4. https://doi.org/10.1103/PhysRevLett.97.253904

27. Fan B, Liu F, Li Y et al (2012) Refractive Index Sensor Based on Hybrid Coupler with Short-range Surface Plasmon Polariton and Dielectric Waveguide. Appl Phys Lett 100:111108. https://doi.org/10.1063/1.3693408

28. Fan B, Liu F, Wang X et al (2013) Integrated Sensor for Ultra-thin Layer Sensing Based on Hybrid Coupler with Short-range Surface Plasmon Polariton and Dielectric Waveguide. Appl Phys Lett 102:061109. https://doi.org/10.1063/1.4792319

29. Swiech W, Fecher G, Ziethen C et al (1997) Recent Progress in Photoemission Microscopy with Emphasis on Chemical and Magnetic Sensitivity. J Electron Spectros Relat Phenomena 84:171–188. https://doi.org/10.1016/S0368-2048(97)00022-4

30. Lemke C, Leißner T, Klick A et al (2013) The Complex Dispersion Relation of Surface Plasmon Polaritons at Gold/Para-hexaphenylene Interfaces. Appl Phys B 116:585–591. https://doi.org/10.1007/s00340-013-5737-2

31. Olmon RL, Slovick B, Johnson TW et al (2012) Optical Dielectric Function of Gold. Phys Rev B 86:235147. https://doi.org/10.1103/PhysRevB.86.235147

32. Schindelin J, Arganda-Carreras I, Frise E et al (2012) Fiji: An Open-source Platform for Biological-image Analysis. Nat Methods 9:676–682. https://doi.org/10.1038/nmeth.2019

33. Edelstein A, Amodaj N, Hoover K et al (2010) Computer Control of Microscopes Using μManager. Curr Protoc Mol Biol Chapter 14(Unit14):20. https://doi.org/10.1002/0471142727.mb1420s92

34. Joens MS, Huynh C, Kasuboski JM et al (2013) Helium Ion Microscopy (HIM) for the Imaging of Biological Samples at Sub-nanometer Resolution. Sci Rep 3:3514. https://doi.org/10.1038/srep03514

35. Klick A, de la Cruz S, Lemke C et al (2016) Amplitude and Phase of Surface Plasmon Polaritons Excited at a Step Edge. Appl Phys B 122:79. https://doi.org/10.1007/s00340-016-6350-y

36. Cardona M (1971) Fresnel Reflection and Surface Plasmons. Am J Phys 39:1277–1277. https://doi.org/10.1119/1.1976627

37. Burke JJ, Stegeman GI, Tamir T (1986) Surface-polariton-like Waves Guided by Thin, Lossy Metal Films. Phys Rev B 33:5186–5201. https://doi.org/10.1103/PhysRevB.33.5186

38. Foley JJ IV, Harutyunyan H, Rosenmann D et al (2015) When are Surface Plasmon Polaritons Excited in the Kretschmann-Raether Configuration? Sci Rep 5:9929. https://doi.org/10.1038/srep09929

39. Davis TJ (2009) Surface Plasmon Modes in Multi-layer Thin-films. Opt Commun 282:135–140. https://doi.org/10.1016/j.optcom.2008.09.043

40. Malitson IH (1965) Interspecimen Comparison of the Refractive Index of Fused Silica*,†. J Opt Soc Am 55:1205. https://doi.org/10.1364/JOSA.55.001205

41. Green MA (2008) Self-consistent Optical Parameters of Intrinsic Silicon at 300K Including Temperature Coefficients. Sol Energy Mater Sol Cells 92:1305–1310. https://doi.org/10.1016/j.solmat.2008.06.009

42. Rodríguez-de Marcos LV, Larruquert JI, Méndez JA, Aznárez JA (2016) Self-consistent Optical Constants of SiO_2 and Ta_2O_5 Films. Opt Mater Express 6:3622. https://doi.org/10.1364/OME.6.003622

43. Morita M, Ohmi T, Hasegawa E et al (1990) Growth of Native Oxide on a Silicon Surface. J Appl Phys 68:1272–1281. https://doi.org/10.1063/1.347181

44. Chu WK, Lugujjo E, Mayer JW, Sigmon TW (1973) Line-shape Extraction Analysis of Silicon Oxide Layers on Silicon by Channelling Effect Measurements. Thin Solid Films 19:329–337. https://doi.org/10.1016/0040-6090(73)90069-2

45. Philipp HR, Taft EA (1982) An Optical Characterization of Native Oxides and Thin Thermal Oxides on Silicon. J Appl Phys 53:5224–5229. https://doi.org/10.1063/1.331401

46. Kim MJ, Carpenter RW (1990) Composition and Structure of Native Oxide on Silicon by High Resolution Analytical Electron Microscopy. J Mater Res 5:347–351. https://doi.org/10.1557/JMR.1990.0347

47. Lin C-H (2013) Oxidation (of Silicon). In: Li D (ed) Encyclopedia of Microfluidics and Nanofluidics. Springer, US, Boston, MA, pp 1–11

48. Seah MP, Dench WA (1979) Quantitative Electron Spectroscopy of Surfaces: A Standard Data Base for Electron Inelastic Mean Free Paths in Solids. Surf Interface Anal 1:2–11. https://doi.org/10.1002/sia.740010103

49. Drezet A, Hohenau A, Koller D et al (2008) Leakage Radiation Microscopy of Surface Plasmon Polaritons. Mater Sci Eng B 149:220–229. https://doi.org/10.1016/j.mseb.2007.10.010

50. Grainger DW, Castner DG (2011) 3.301 - Surface Analysis and Biointerfaces: Vacuum and Ambient in Situ Techniques. In: Ducheyne PBTCB (ed). Elsevier, Oxford, pp 1–22

51. Gjonaj B, Aulbach J, Johnson PM et al (2013) Focusing and Scanning Microscopy with Propagating Surface Plasmons. Phys Rev Lett 110:28–32. https://doi.org/10.1103/PhysRevLett.110.266804